Supplementary Information

Space-Time Wavefront Synchronized Optoelectronics

Chiben Zhang[1,8], Jing Lou[2,3,8], Jing Zhang[1], Zhuochao Wang[4], Chang-Yin Ji[4], Yindong Huang[2], Zhenfei Li[5], Weiren Zhu[6], Longyue Li[1], Longqing Cong[7]*, Guangwei Hu[4]*, and Chao Chang[2,3]**

[1]*Air and Missile Defense College, Air Force Engineering University, Xi'an, China*
[2]*Innovation Laboratory of Terahertz Biophysics, National Innovation Institute of Defense Technology, Beijing, China*
[3]*School of Physics, Peking University, Beijing, 100871, China*
[4]*School of Electrical & Electronic Engineering, Nanyang Technological University, Singapore, Singapore*
[5]*School of Physical Science and Technology, Northwestern Polytechnical University, Xi'an, China*
[6]*Department of Electronic Engineering, Shanghai Jiao Tong University, Shanghai, China,*
[7]*Department of Electrical and Electronic Engineering, Southern University of Science and Technology, Shenzhen, China*
[8]*These authors contributed equally: Chiben Zhang, Jing Lou*
**Corresponding author: gwyzlzssb@pku.edu.cn, loujing9486@163.com, conglq@sustech.edu.cn, guangwei.hu@ntu.edu.sg*

S1 Enhanced overlap of optical pump-excited local fields with EM-excited local fields

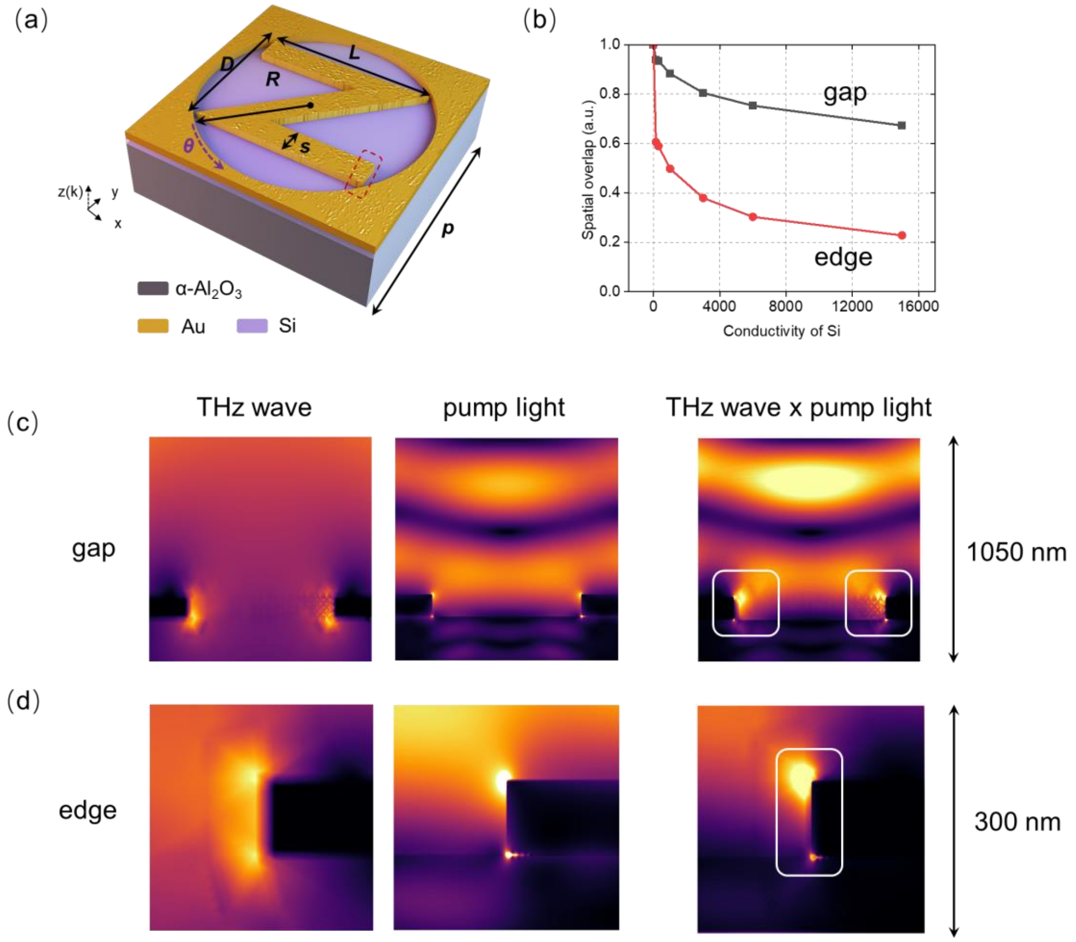

Figure S1 Configuration and resonance performance for the OEM array. (a) A unit cell is constructed by a modified Z-shaped structure with the geometrical parameters given by $L =$ 58.5 μm, $D =$ 44.5 μm, $s =$ 8 μm, $R =$ 38 μm and $p =$ 80 μm. The inset picture is a side view showing the charge motion processes resulting from resonance and optical excitation. (b) Spatial overlap between the optical and terahertz beams is a function of terahertz frequency in the gap and edge regions, which both cause an exponential decrease in the overlap of the two as the conductivity increases. The electric field profile at $\lambda = 800\,nm$, The electric field profile at $f = 0.6$ THz, and the multiplication product of the optical absorption and electric field profiles within a 100 nm depth in the Si substrate in (c)gap and (d)edge.

To further explore the role of the optical pump excitation local strong field in EM resonant modulation, we calculate the local field distributions in the gap and edge regions under EM excitation by simulation, respectively, as shown in Figure S1, under excitation, the stronger localized fields are generated in both the metal regions above the dielectric layer and below the air layer in the gap structure. Here, to characterize the coupling effect between the strong local field distributions of optical pumping and terahertz excitation, we perform a normalized combined calculation of their local fields. We can clearly observe that the electromagnetic field distributions under different frequency bands of excitation possess a high degree of overlap, which leads to an enhanced coupling between the two, thus realizing the emphasized phenomenon at low pump energies. At the beginning of the silicon conductivity increase, which also implies low-pump-energy light incidence, both for gap and edge region, slight variations cause an extremely large decrease in the terahertz and optical field overlap rates that prove our proposed OEM arrays have sensitive modulation properties. Moreover, the same trend is exhibited in the edge region. Therefore, utilizing this edge-enhanced local field coupling enhancement effect, the EM platform possesses extremely high optical sensitivity, which is expected to promote the development of low-energy and high-efficiency devices.

S2 Symmetry for the unit cell of OEM array

The OEM array designed in the article exhibits functional symmetry for both σ+ and σ- incidence, which is determined by the rotational symmetry of the unit cell. However, for certain asymmetric application scenarios, it is required to exhibit polarization asymmetry. Here, an asymmetric unit cell with chiral selectivity is designed based on the unit cell of the OEM array. As shown in Figure S2(a), the asymmetric unit cell introduces structural asymmetry based on the rotationally symmetric Z-shaped unit cell, which can be viewed as a portion of metal being subtracted from the lower right corner of the Z-shaped cell with a length of d. When a σ+ wave is incident on the unit cell in the $+z$ direction, the Z-shaped resonator undergoes violent resonance, inducing an ohmic loss, which causes a large amount of the electromagnetic wave to be dissipated inside the cell, thus absorbing the σ- wave. On the other hand, when the polarization of the circularly polarized incident wave becomes σ-, the Z-shaped resonator is not excited to resonate strongly, as shown in Fig. Figure S2(b). The above phenomenon can be confirmed by observing the inductive current at the resonance point, as shown in Figure S2(c) and (d), respectively.

Observation of the red transmission curves in Figure S2(e) and (f) shows that there is a clear transmission valley in the transmission spectral line at the incidence of σ+ waves, which is almost zero at the lowest point. In contrast, the amplitude does not change much at the same frequency at the incidence of σ- waves. Further, the multipole decomposition of the asymmetric unit cell at the same resonance point is calculated for both cases, and the comparison shows that compared with the σ- wave incidence case, the magnetic dipole $\mathbf{M}$ and the electric quadrupole $\mathbf{Q_e}$ reach a maximum at the resonance point for the σ- wave incidence case, and even exceed the original second contribution of the ring dipole $\mathbf{T}$, which implies that the change of the asymmetric structure changes the resonance field distribution at the resonance point mainly because caused by the magnetic dipole $\mathbf{M}$ and the electric quadrupole $\mathbf{Q_e}$.

Further, when *d* is varied, Figures S3 (a-b), (c-d), and (e-f) show the transmission, reflection, and absorption curves for the two incident wave scenarios in comparison, respectively. It can be seen that when the σ+ wave is incident, the asymmetric unit cell shows a significant decrease in both transmission and reflection amplitudes at the resonance point, which is due to the absorption by the magnetic dipole $\mathbf{M}$ and the electric quadrupole $\mathbf{Q_e}$. When σ- waves are incident, the transmission and reflection amplitudes do not change much, which is due to the excitation of the larger magnetic dipole $\mathbf{M}$ and electric quadrupole $\mathbf{Q_e}$ in this case, and it can be seen from the parameter scanning of *d* that when σ+ waves are incident, the resonance valley deepens or weakens with the length of *d*, and reaches a maximum value close to 0 when it reaches 7 μm, which means that the asymmetric unit cell can respond to terahertz waves at the resonance point in both the transmission mode and the reflection mode. Resonance point to achieve better asymmetric transmission of waves, i.e., when encountering σ+ waves, the waves are strongly absorbed, while σ- waves are incident without large changes in the amplitude, and the design of wave phase modulation is still possible.

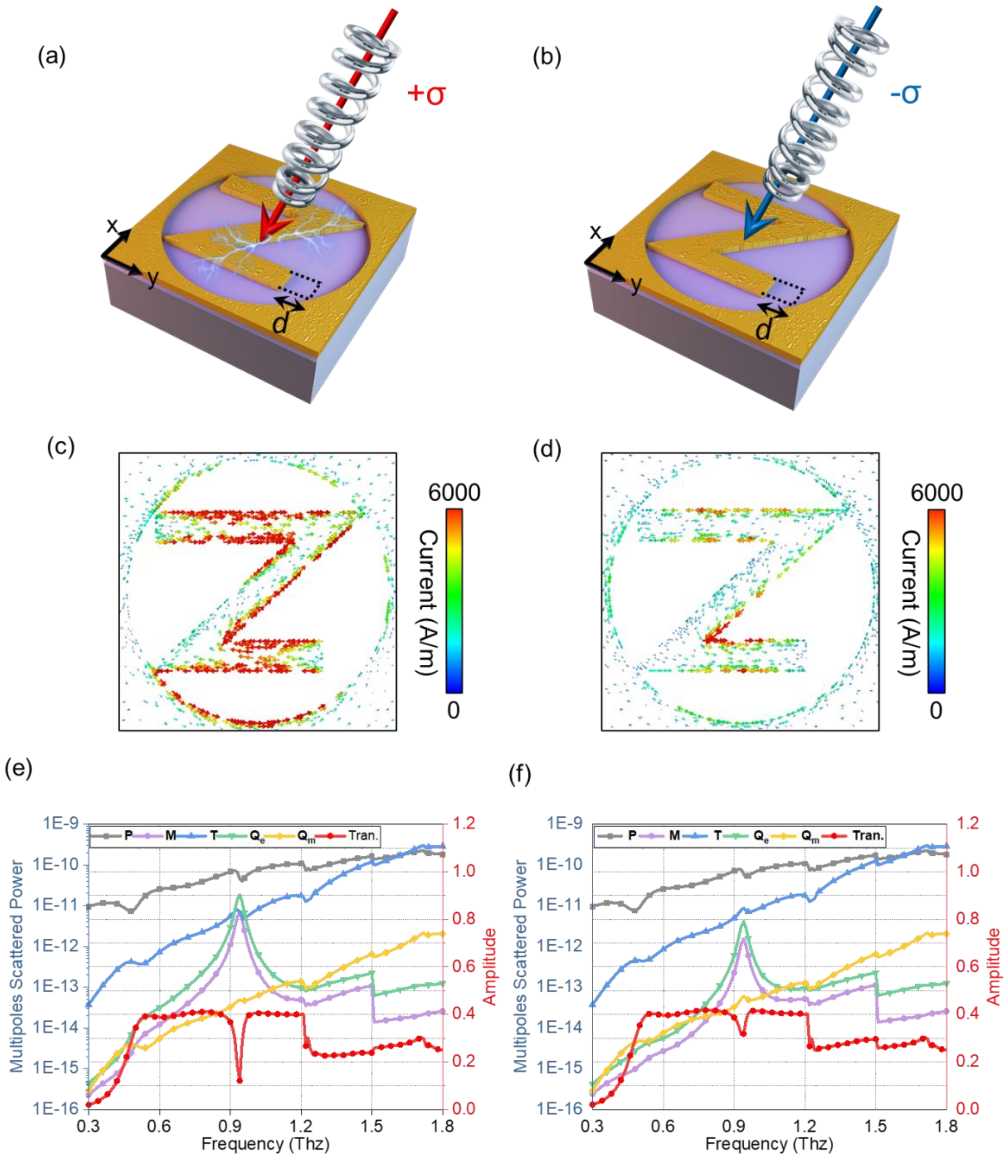

Figure S2 Asymmetric unit cell of OEM array. (a) Schematic of σ+ incident asymmetric unit cell, (b) Schematic of σ- incident asymmetric unit cell, (c) Surface current distribution at σ+ incidence, (d) Surface current distribution at σ- incidence, (e) Multipole scattering energy distribution at σ+ incidence, and (f) Multipole scattering energy distribution at σ-incidence.

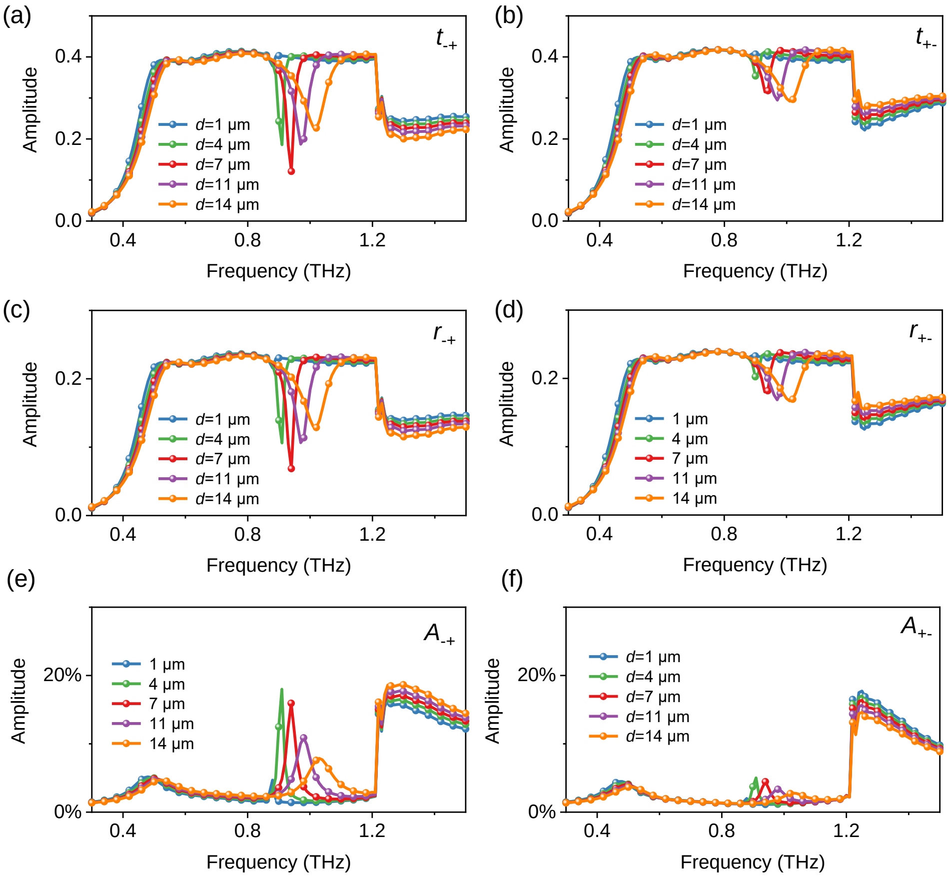

Figure S3 Transmission, reflection, and absorption performance of asymmetric unit cells at different *r*. (a) Transmission amplitude at $\sigma+$ incidence, (b) transmission amplitude at $\sigma-$ incidence, (c) Reflection amplitude at $\sigma+$ incidence, (d) reflection amplitude at $\sigma-$ incidence, (e) absorption at $\sigma+$ incidence, (f) absorption at $\sigma-$ incidence.

S3 Comparison of regular and modified Z-shaped unit cells

We investigate the radiative properties of the two unit cells proposed by regular Z-shaped (Figures S4(a)) and (Figures S4(c)) modified Z-shaped structures via simulated surface currents at the characteristic resonance frequencies when they are illuminated in Figures S4(b) and S4(d). For a Z-shaped resonator, the current flows along the longest Z-shaped path at 0.62 THz, which means that this mode has the minimum resonant frequency $f_{\min}$ when having the maximum equivalent inductance according to equivalent circuit theory[1]. As the frequency increases, the resonance intensity is weakened, as demonstrated at 0.85 THz, which is manifested by a decrease in amplitude. However, as the spectrum is further blue-shifted, another new mode occurs with three separated currents directed in different directions at 1.21 THz. It improves the amplitude, but there still appears to be an amplitude dip due to the absence of a transition mode between it and the previous mode. Therefore, we address the above problem by introducing an extra mode by modifying the conventional Z-shaped structure. There are two enhancements for manipulation; one is that the operation bandwidth is extended to start from 0.51 THz, as seen in Figure 4(d) since the circumscribed hole delivers a longer path to the current can flow compared to a Z-shaped structure. The other is that both transmission and reflection amplitude are flattened owing to the emergence of new modes in a modified Z-shaped structure, which is extrinsically characterized by the emergence of extra currents, as shown in Figure S4(d).

For broadband and high-modulation efficiency, we construct an optimized Z-shaped structure as a unit cell of the OEM array. This can support not only the traditional resonance mode of a magnetic dipole (MD) and electric dipole (ED) but also diverse resonances, such as toroidal dipole (TD), to enhance higher modulation efficiencies of EM waves because of their weak free-space coupling. Compared to the regular Z-shaped structure (Figure S2(b)), the extra circumscribed hole could stimulate more inductive currents(Figure S2(d)), resulting in higher-order resonance modes. We calculate and compare the scattered power of the two structures by utilizing the multipole expansion[2][3], as shown in Figure S2(c). Three multipoles contribute the most in terms of scattering power under $\sigma+$ wave illumination, namely ED, TD, and magnetic quadrupole (MQ). As an example, the scattering power of ED can be expressed as $\frac{2\omega^4}{3c^3}|\mathbf{P}|$, where **P** is the ED moment. The formula $\mathbf{P} = \frac{1}{i\omega}\int \mathbf{j}\boldsymbol{d^3r}$ is used to calculate **P**, where **j** and **r** are the current density and the displacement vectors, respectively (see Supplementary Section 4 for more details). The results show that both unit cells are mainly contributed by the three dominant multipoles where ED dominates. Therefore, the minimum resonant frequency $f_{\min}$ for the unit cell depends on the maximum length $l_{\max}$ emerges for flowing current on it, following the relation $f \propto 1/l$. Besides, all poles are exponentially enhanced in modified Z-shaped structures, especially TD and MQ modes, since more complex field architectures are built, as shown in Figure S1d, which facilitates the modulation of electromagnetic waves owing to stronger light-matter interactions.

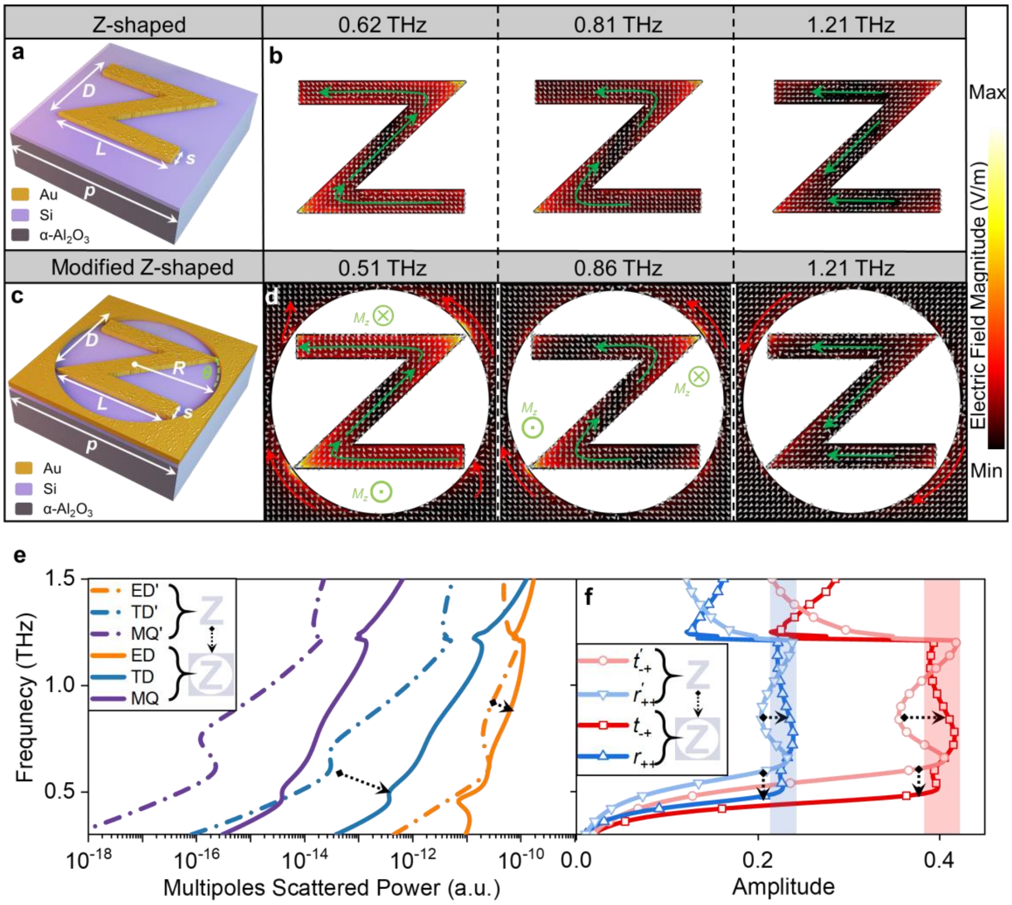

Figure S4 Comparison of regular and modified Z-shaped unit cells. Model of (a) regular Z-shaped and (c) modified Z-shaped structure. The rotation angle along the center of the Z-shaped structure is θ. The surface current distribution of (b) regular and (d) modified Z-shaped structure at 0.62, 0.85, 1.21 THz and 0.52, 0.85, 1.21THz, respectively.

S4 Multipole expansion calculation

To further quantitatively understand the resonances of unit cells, the multipole expansion of scattered power (*I*) is calculated based on Taylor expansion of charge and current densities, including the magnitude of electric and magnetic multipoles, as well as toroidal dipole as follows[4]:

$$I = \frac{2\omega^4}{3c^3}|\mathbf{P}|^2 + \frac{2\omega^4}{3c^3}|\mathbf{M}|^2 + \frac{4\omega^5}{3c^4}|\mathbf{P}\cdot\mathbf{T}|^2 + \frac{\omega^6}{5c^5}\sum_{\alpha,\beta}\left|Q_e^{\alpha\beta}\right|^2 + \frac{\omega^6}{40c^5}\sum_{\alpha,\beta}\left|Q_m^{\alpha\beta}\right|^2 \tag{1}$$

where c is the light speed, ω is the angular frequency. In which the multipoles $\mathbf{P}$, $\mathbf{M}$, $\mathbf{T}$, $\mathbf{Q}_e$, and $\mathbf{Q}_m$ are electric dipole (ED), magnetic dipole (MD), toroidal dipole (TD), electric quadrupole (EQ), and magnetic quadrupole (MQ), respectively. They can be expressed as follows:

$$\mathbf{P} = \frac{1}{i\omega}\int \mathbf{j}\boldsymbol{d^3r} \tag{2}$$

$$\mathbf{M} = \frac{1}{2c}\int \mathbf{r}\times\mathbf{j}\boldsymbol{d^3r} \tag{3}$$

$$\mathbf{T} = \frac{\mathbf{1}}{10c}\int [(\mathbf{r}\cdot\mathbf{j})\mathbf{r} - 2\mathbf{r}^2\mathbf{j}]\boldsymbol{d^3r} \tag{4}$$

$$Q_e^{\alpha\beta} = \frac{1}{i\omega}\int\left[r_\alpha j_\beta + r_\beta j_\alpha + \frac{2}{3}\boldsymbol{\delta_{\alpha\beta}}\mathbf{r}\cdot\mathbf{j}\right]\boldsymbol{d^3r} \tag{5}$$

$$Q_m^{\alpha\beta} = \frac{1}{3c}\int [(\mathbf{r}\times\mathbf{j})_{\boldsymbol{\alpha}} r_\beta + (\mathbf{r}\times\mathbf{j})_{\boldsymbol{\beta}} r_\alpha]\boldsymbol{d^3r} \tag{6}$$

where $\mathbf{j}$ and $\mathbf{r}$ are the induced current density and the location at which the induced current density is evaluated, respectively, the dispersion of scattered power for various multipole moments is calculated by Matlab programs and *LiveLink for the Matlab* feature of Comsol Multiphysics.

S5 Experimental transmission and reflectance with increasing pump fluence

In the experiment, the effect of the accompanying pump light fluence on the transmission spectral lines was also investigated. We constructed isotropic arrays (200 × 200 unit cells) to examine the performance of unit amplitude modulation with x/y-polarized wave incidence and y/x-polarized wave incidence, where circular polarization (σ+/-) be synthesized by the two mutually perpendicular electric field components, as shown in Figure S5(a). As the increase of pump light from 0 to 100 μJ/cm², the amplitude is gradually decreased to nearly zero at 0.51-1.21 THz both for transmission and reflection waves (Figure S5(b) and (c)), since the resonance filed is weakened, as shown in the Figure S5(d), respectively. The experimental results match the simulation results

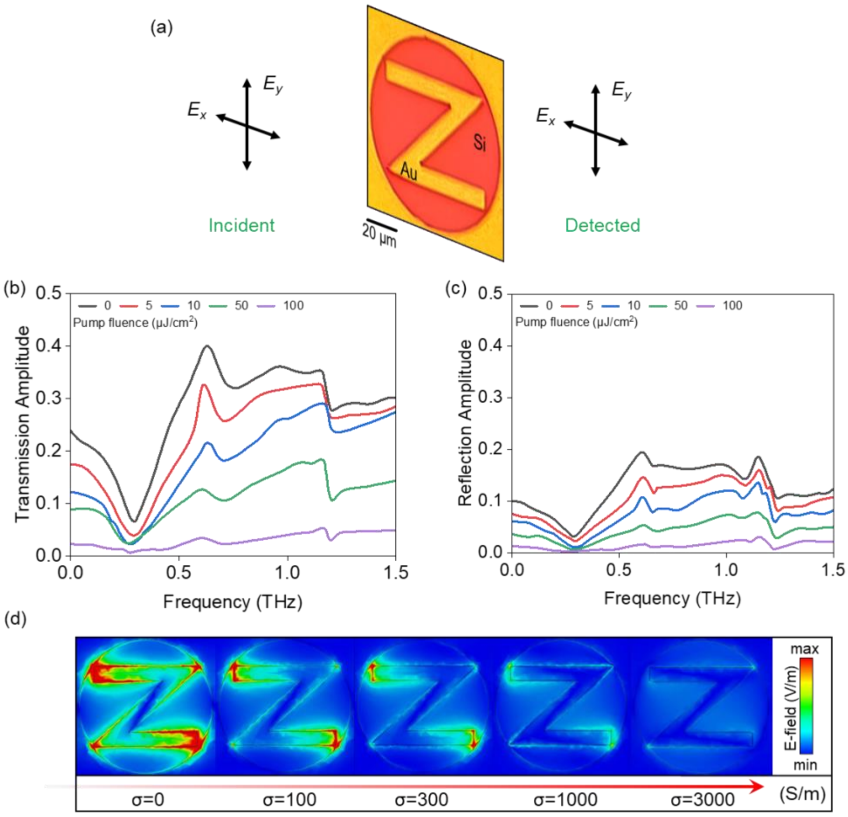

Figure S5 Unit cell of OEM array variation with pump fluence. (a) Test schematic by *the x/y*-polarized transmitter and *x*/*y*-polarized receiver with the unit cell microscope diagram in the middle, where The circularly polarized signals are synthesized from linear polarization. (b) measured S21 variation with conductivity, (c) simulated S21 variation with optical pump fluence and (d) electric field intensity variation with conductivity. The modulation depth of transmitted ($T = |t_{-+}|^2$) and reflected energy ($R = |r_{++}|^2$) can reach >98% and >95% at 0.51-1.21 THz, respectively, characterized as $\frac{T_{\sigma=0}-T_{\sigma=3000}}{T_{\sigma=0}}$ and $\frac{R_{\sigma=0}-R_{\sigma=3000}}{R_{\sigma=0}}$. (d) E-filed variation with conductivity of Si increased, corresponding the pump fluence enhanced.

S6 Phase offsets performance when σ_{Si}=3000 S/m

In the main article, Figure 2f shows that the reflected and transmitted PB phases are found to be the same in the absence of pump light irradiation, and both have good stability (within ±5°). Further, we simulate that with the increase of pump fluence (conductivity of Si σ_{Si}), the phase is still controlled within a good fluctuation range of ±5°, e.g., at σ_{Si}=3000 (Figure S6), which facilitates the independent tuning of the wavefront and energy after grouping the arrays according to the phase distribution.

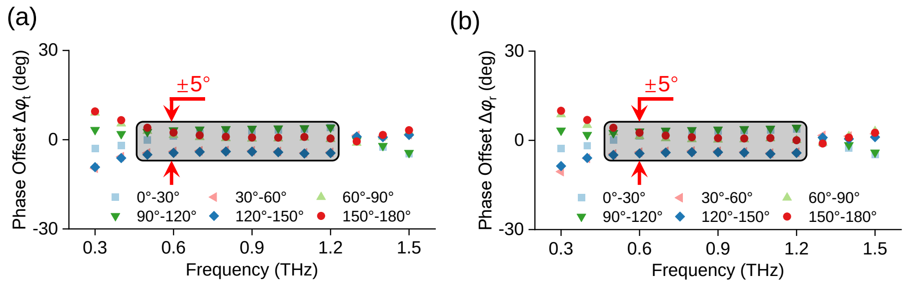

Figure S6. Phase offsets performance when σ_{Si}=3000 S/m for (a)transmission and (b)reflection.

S7 Frequency-dependent photoconductivity in Si at different pump fluences.

Tests were performed to obtain a broadband representation of the silicon conductivity σ_{Si} with respect to the pump fluence, as shown in the inset of Figure S7, where it can be seen that the silicon film fluctuates less in the broadband range, being overall smoother. In more detail, the photoconductivity σ_{Si} at 0.5, 1, and 1.5 THz is extracted. Observation of Figure 3.8(a) reveals that the silicon film conductivity all grows logarithmically with the pump light energy density from 0 to 1600 μJ/cm^2 in line with the logarithmic growth, specifically from near 100 S/m to about 15000 S/m.

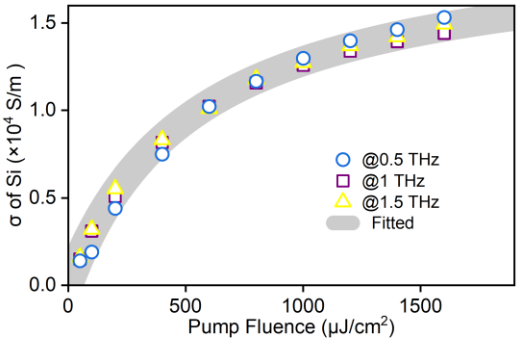

Figure S7 Experimentally retrieved frequency-dependent photoconductivity at different pump fluences.

S8 Stable phase independent regulation

The OEM array can realize 360° modulation of the transmitted and reflected phases simultaneously. According to the PB phase theory, when the incident wave is pure σ+/-, the modulated wave exhibits opposite chirality (σ-/+ for transmission and σ+/- for reflection) as well as strict adherence to the $\pm 2\theta$ phase difference in the same coordinate reference system as shown in Figure S8(a) and (b) θ is the angle of rotation of the Z-shaped structure around its center. When the θ rotation is 180° from 0°, the phase undergoes a full phase modulation from 0° to 360° for transmitted waves, while for reflected waves, the modulation phase takes negative and undergoes a full phase modulation from 0° to -360° due to the steering of the vector direction in the same coordinate system. Specifically, taking the rotation angles of 0°, 30°, 60°, 90°, 120°, 150°, and 180° yields the transmission phase (Figure S8(c)), reflection phase (Figure S8(d)), transmission amplitude (Figure S8(e)), and reflection amplitude (Figure S8(f)) of the unit cell. It is observed that the transmission phase difference $\Delta\varphi_t$ and reflection phase difference $\Delta\varphi_r$ of their neighboring rotation angles are both about 60°, i.e., $2\Delta\theta$, which coincides with the PB theorem. At the same time, their corresponding amplitudes do not change.

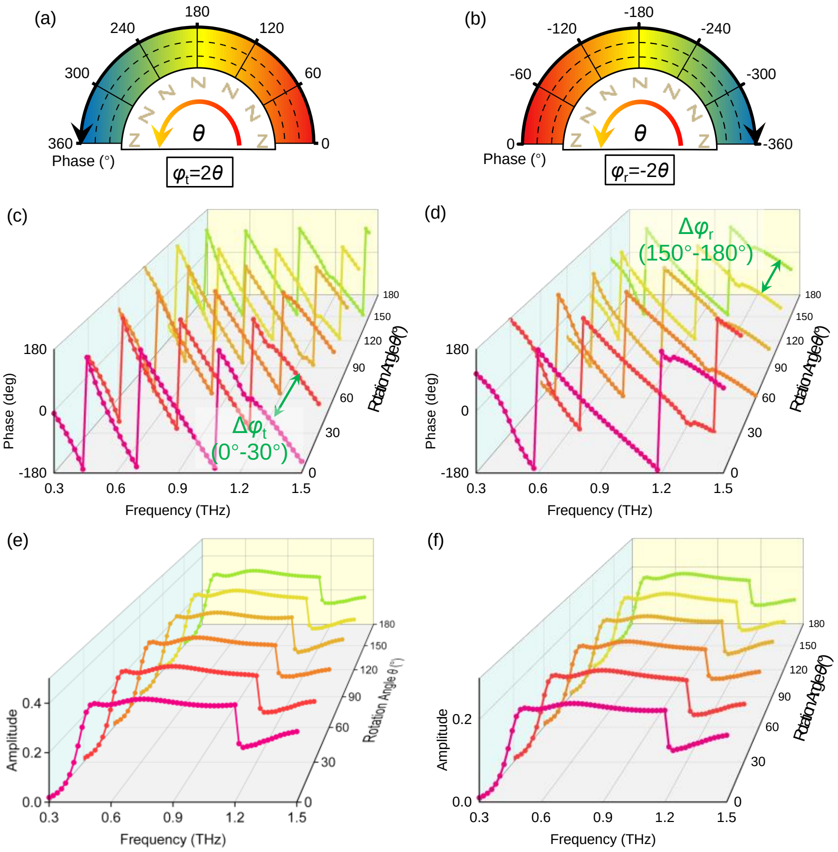

Figure S8 Variation of amplitude and phase with rotation angle θ. (a)Transmission and (b)reflection phase. (c) Transmitted and (d)reflection amplitude. (e)Transmission and (f)reflection phase.

S9 Amplitude-phase independent control of OEM array

The resonant strength of the metallic resonator is attenuated, as shown by the gradually decreasing electric field (Figure S9(a)), which affects the scattering amplitude and phase for transmitted and reflected waves. Under the pump light fluence of $1600\ \mu\mathrm{J/cm^2}$, the conductivity is about $15000\ \mathrm{S/m}$; at this time, the transmission and reflection amplitudes are close to 0, and the modulation depth is close to 100% by calculation. By observing the transmission curve (Figure S9(b)) and reflection curve (Figure S9(c)), it can be seen that when the conductivity is greater than $3000\ \mathrm{S/m}$, the amplitude of the two has been at a lower level and changes slowly. By calculating the transmittance T_{-+} and reflectance R_{++} of the modulated wave in more detail, when the conductivity of the silicon film is increased from 100 to $3000\ \mathrm{S/m}$, the OEM array is already able to achieve a high modulation depth of $97\% \sim 83\%$ in the broadband range of $0.51\text{-}1.21$ THz, and the pumping threshold is only $100\ \mu\mathrm{J/cm^2}$ at this time. Moreover, the modulation depth can reach 100% when the conductivity of Si improved to $15000\ \mathrm{S/m}$, as shown in Figure S6(f) and (g). For the phase, as shown in Figure S6(d) and (e), although the phase is shifted when the conductivity of the silicon film changes, the phase shift is the same for each cell for the OEM array as a whole due to the uniform distribution of the scale across the entire surface, so the phase change does not affect the array wavefront modulation, but only has an effect on the amplitude.

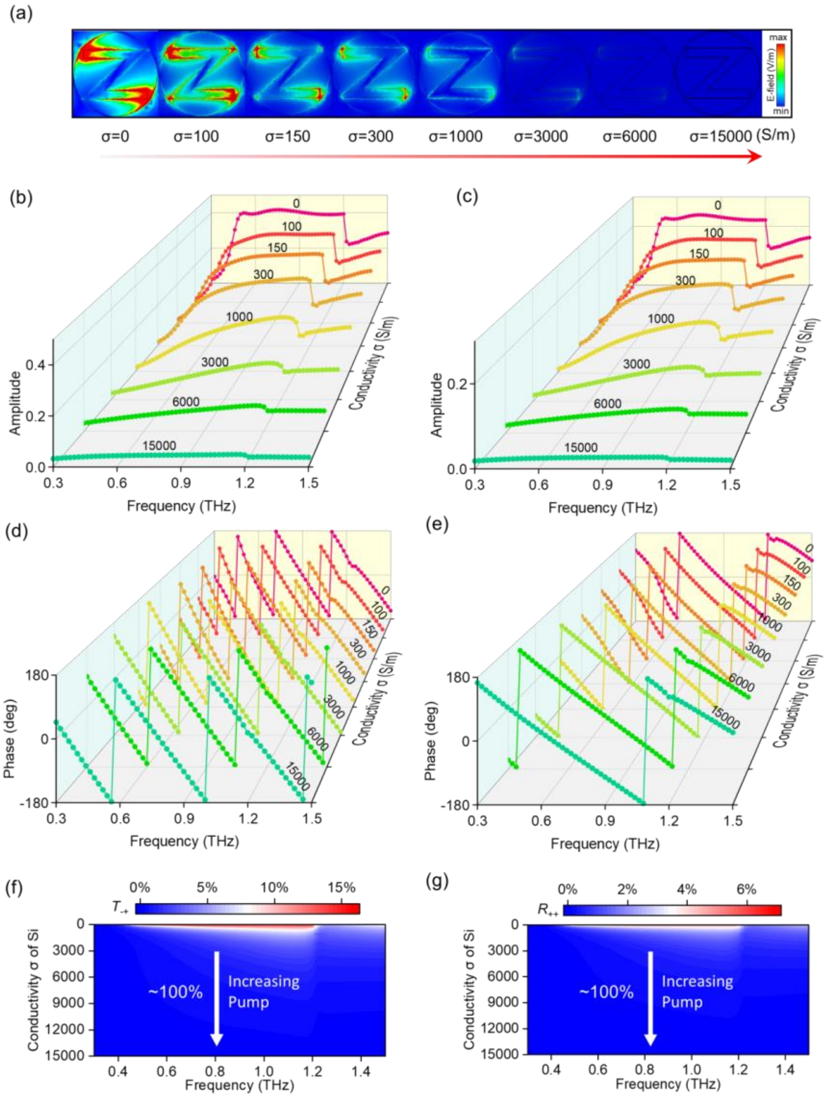

Figure S9 Variation of transmission and reflection amplitude of unit cell with silicon conductivity. (a) Effect of different conductivities on E-field. (b) Effect of different conductivities on transmission amplitude. (c) Effect of different conductivities on reflection amplitude. (d) Effect of different conductivities on transmission phase. (e) Effect of different conductivities on reflection phase. (f) Broadband effect of conductivity variation on transmission energy. (g) Broadband effect of conductivity variation on reflection energy. The modulation depth of transmitted ($T = |t_{-+}|^2$) and reflected energy ($R = |r_{++}|^2$) can reach 97%-83% at 0.51-1.21 THz, characterized as $\frac{T_{\sigma=0}-T_{\sigma=3000}}{T_{\sigma=0}}$ and $\frac{R_{\sigma=0}-R_{\sigma=3000}}{R_{\sigma=0}}$. Moreover, the modulation depth ($\frac{T_{\sigma=0}-T_{\sigma=15000}}{T_{\sigma=0}}$, $\frac{R_{\sigma=0}-R_{\sigma=15000}}{R_{\sigma=0}}$) can reach 100% both for transmission and reflection waves when the conductivity of Si improved to 15000 S/m

S10 Efficiency limits and Bragg reflections effect the performance of OEM array

In fact, we could have obtained higher modulated wave amplitudes and wider bandwidths, yet here, it is theoretically limited by Bragg reflections[5]. For amplitude, the OEM array is described by the scattering matrix of a four-port system with an input and output port for each polarization (σ_+andσ_-). The following equations basically restrict the amplitude of the circular cross-coupling transmission efficiency t_{-+} and reflection efficiency r_{++}. They can be described as

$$|t_{-+}| = Re(t_{--}) - |t_{--}|^2, \qquad |r_{++}| = Re(r_{+-}) - |r_{+-}|^2 \tag{7}$$

where we take the σ_+ incident wave as an example.

Consider the OEM array described by the scattering matrix of a four-port system with an input $\sigma_+$and output port σ_- for each polarization[6]. Under this condition, the amplitudes of t_{-+} and r_{++} are exclusively determined by the co-polarization transmission efficiency t_{++} and r_{+-}. and the maximum cross-coupling efficiency $\frac{|t_{-+}|^2}{|r_{++}|^2}$ in half space is 0.25. They also possess simultaneity and even equivalence as the boundary conditions in transmission and reflection space are the same, owing to the symmetry in terms of polarization and spatial based on the Pancharatnam–Berry (PB) phase or geometric phase theory.

For a periodic lattice, there exists$\Delta\mathbf{k} = \mathbf{k}^{'} - \mathbf{k} = \mathbf{G}$, where $\mathbf{k}$ and $\mathbf{k}'$are the wave vectors of the incident and scattered waves, respectively, and $\boldsymbol{G}$ is a vector of the reciprocal lattice. Namely, for a rectangular planar array of scatterers with fundamental translations, $a_1 = a\hat{x}$, $a_2 = a\hat{y}$, and the basis of the corresponding reciprocal lattice is formed by $b_1 = \frac{2\pi}{a}\hat{x}$ and $b_2 = \frac{2\pi}{a}\hat{y}$. The last vectors can be used to expand all reciprocal lattice vectors $\boldsymbol{G} = n_1 b_1 + n_2 b_2$, where n_1 and n_2 are integer numbers. Substitution of the last result into the diffraction condition leads to the next conditions for Bragg reflections:

$$\sin\theta^{'}\cos\phi^{'} - \sin\theta\cos\phi = n_1\frac{\lambda}{a} \tag{8a}$$

$$\sin\theta^{'}\sin\phi^{'} - \sin\theta\sin\phi = n_2\frac{\lambda}{a} \tag{8b}$$

where θ, ϕ, θ', and ϕ are the angular spherical coordinates of the wave vectors $\mathbf{k}$ and $\mathbf{k}$‘, respectively. By taking absolute values on both sides of (8) and looking for the maximum of the left side, it is easy to demonstrate that a Bragg reflection of order(n_1, n_2) can only happen when $\frac{|n_1|\lambda}{a} \leq 2$ and$\frac{|n_2|\lambda}{a} \leq 2$. Therefore, it is impossible to fulfill both conditions at the same time when$\lambda > 2\,max\,(a, b)$, unless$n_1 = n_2 = 0$, which corresponds to the conventional ray transmitted along the incidence direction or the ray suffering a conventional mirror reflection. Especially for the case of normal incidence and $a = p$, it is easy to see from (1) that Bragg reflections in the non-magnetic isotropic medium are avoided when $\lambda' > p$, where $\lambda'$is the equivalent wavelength can be calculated as $\frac{\lambda}{\sqrt{\varepsilon}}$.

For the broadband performance to be fully exploited in the design of monolayer OEM arrays, the condition $f_{max} < \frac{c}{p\sqrt{\varepsilon}}$ is derived under the condition of a non-magnetic isotropic medium, where maximum operation frequency f_{max} is determined by the structure confined to the lattice with period p. The best case for the above inequality is that the left term is as large as possible, and the right term is as tiny as possible. However, they do not vary independently due to the contradiction arising from the p that both exist. Therefore, the choice of the substrate in designing the broadband OEM array is significant to keep permittivity as small as possible, just as in case $\varepsilon = 1$, there is no Bragg scattering due to not reaching the threshold shown in the dashed line in Figure S10(a) and (b).

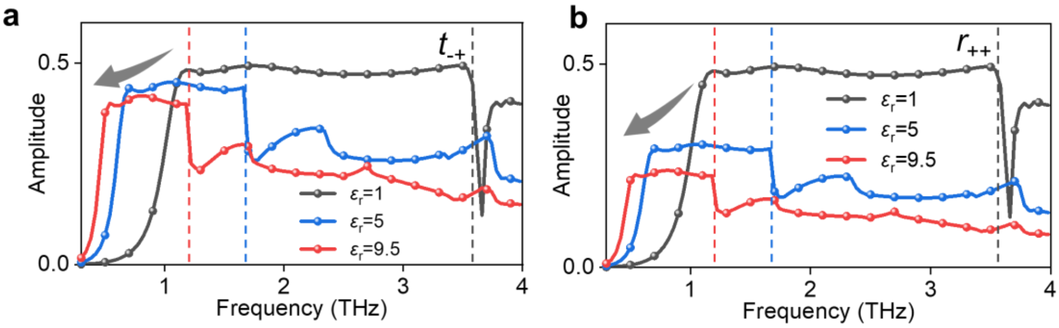

Figure S10. Influence of dielectric substrate on bandwidth and amplitude for (d) transmission and (e) reflection. It is worth noting that since the direction of the reflected wave vector is reversed, r_{++} also represents the cross-polarization as t_{-+}. When the permittivity is 1, it can be regarded as a vacuum.

Different from the PB structure as a half-wave plate in refs.[7][8], our single-layer structure achieves flat amplitude curves in the broadband range via multipolar resonances, as shown in Figure S10. However, amplitude drops and the introduction of dielectrics can lead to shrinking of the operating bandwidth since the substrate will degrade performance due to the broken symmetry of the whole configuration along *the* z-axis. The transmitted and reflected curves with different permittivity ε with values of 1 (air), 5, and 9.5 (α-Al_2O_3) were simulated. We find that the bandwidth is compressed by a factor of $\sqrt{\varepsilon}$, resulting from the scaling of the optical path in the medium for regular and modified Z-shaped structures. Meanwhile, unsmoothed cliff-like drops occur when ε is 5 and 9.5 at the upper boundary, since the formation of diffracted modes owing to Bragg reflections, which follows $f_{max} < \frac{c}{p\sqrt{\varepsilon}}$ as illustrated by dashed lines (see more details in Supplementary Section 5). Amplitude deterioration is a result of multiple scattering and dielectric losses in the interfaces. In summary, after delicate parameter optimization of the modified Z-shaped unit cell, flat transmission and reflection amplitudes with values around 0.42 and 0.24 are obtained, covering the broadband frequency range of 0.51-1.21 THz (81.4% relative bandwidth).

S11 Process of Hologram Optimization Algorithm

Based on the conditions, including imaging distance of 27 mm, frequency of 0.9 THz, and size of 70×70 subarrays, Rayleigh–Sommerfeld diffraction is adopted, which could be formulated as

$$u(x_0,y_0)=\frac{1}{i\lambda}\int u(x,y)\frac{e^{ikr}}{r}dxdy \tag{9}$$

Here, $u\,(x_0, y_0)$ and $u\,(x, y)$ represent the electric fields on the image plane and OEM array plane, respectively, and r represents the distance between two points on them. The inverse process can be formulated as

$$u(x,y)=\frac{1}{i\lambda}\int u(x_0,y_0)\frac{e^{-ikr}}{r}dx_0dy_0 \tag{10}$$

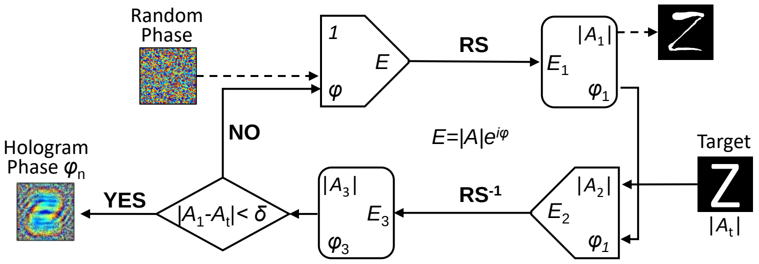

Figure S11. Flowchart of the GS algorithm.

First, the initial electric field reaches the holographic plane by RS diffraction. At this time, the amplitude information is discarded, and the phase information φ_1 is retained. Then, the target amplitude $|A_t|$ is combined with the obtained φ_1 to form a new electric field distributionE_2, where the white part of the graphic letter "Z", for example, is 1, and the black part is 0. Next, an RS inverse transformation is performed on E_2 by following Equation (10) to obtain a new electric field distribution E_3 on the superstructure surface. Next, following Equation (10) to do the inverse transformation of RS to get the new electric field distribution E_3 on the superstructure surface, and finally, the target amplitude $|A_t|$ and the amplitude $|A_1|$ of the phase diffracted through RS on the superstructure surface need to be compared. If the difference between the two is less than the set parameter δ, then the output of the current phase is the desired phase φ_n. If the hologram that has been compared does not have enough similarity with the target graph, the phase needs to be continued to be substituted into the target graph. Then, the phase needs to be substituted into the target graph. Suppose the hologram after comparison does not have enough similarity with the target map. In that case, the phase needs to continue to be substituted into the loop until a phase that meets the requirements is optimized before outputting it again.

S12 Full-space holograms with different conductivity of Si

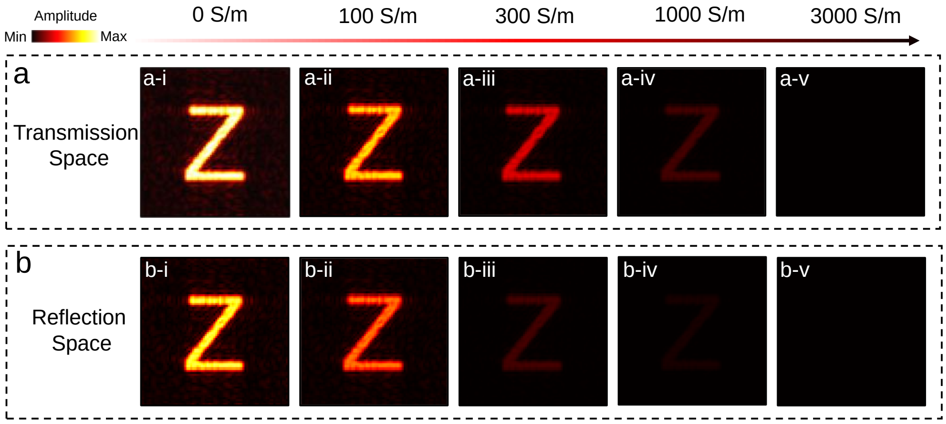

Figure S12. Simulated holograms on (a) transmission and (b) reflection space by increasing σ_{Si} from 0 to 3000 S/m.

We simulated and verified the holographic imaging performance(Figure S12) in the full space; both the reflected hologram and the transmitted hologram can present the obvious target image "Z". With the increase of Si conductivity (corresponding to pump fluence), the brightness of the holographic image will gradually decrease until it is turned off. Further, the normalized holograms of transmission and reflection with different conductivities all have 100% similarity, calculated by the pHash algorithm, which demonstrates that our proposed OEM hologram arrays have perfect synchronized imaging effect and independent programming for wavefront and its energy.

S13 Experimented holograms and its similarity calculation process by pHash algorithm.

We use a comparison algorithm to calculate the similarity between transmission and reflection holograms at different frequencies, as shown in Figure S13. First, we convert the color images to 256-level grayscale to save computation time. Resizing the image to the desired scale of $n \times n$ can further simplify the calculations, where n is denoted by 32, similar to the number of hologram pixels. Secondly, a discrete cosine transform (DCT) is applied to both images. The two-dimensional transformation follows the formula $\mathrm{F(u)} = \mathrm{c(u)}\sum_{\mathrm{i=0}}^{\mathrm{N}-1}\mathrm{f(i)cos}\left[\frac{(\mathrm{i}+0.5)}{N}u\right]$, where $\mathrm{c(u)} = \begin{cases}\sqrt{\frac{1}{N}}, u = 0 \\ \sqrt{\frac{2}{N}}, u \neq 0\end{cases}$, $\mathrm{f(i)}$ is the original signal, $\mathrm{F(u)}$ is the coefficients after DCT, and N is the number of points in the original signal. $\mathrm{c(u)}$ is a compensation coefficient that makes the DCT matrix transformation orthogonal. Then, a $n \times n$ DCT matrix is obtained, while only the information in the low-frequency top-left corner is retained, typically $0.25n \times 0.25n$. The mean matrix of the DCT is calculated and compared with the $0.25n \times 0.25n$ DCT matrix. Values greater than or equal to the DCT mean are set to 1, while values less than the DCT mean are set to 0. The overall structure of the image remains unchanged, and the hash result remains the same. The hash value is then reconstructed by combining $0.25n \times 0.25n$ bits in any order but consistently, resulting in the hash value. Finally, the Hamming distance between the two images is calculated to obtain a specific numerical similarity value.

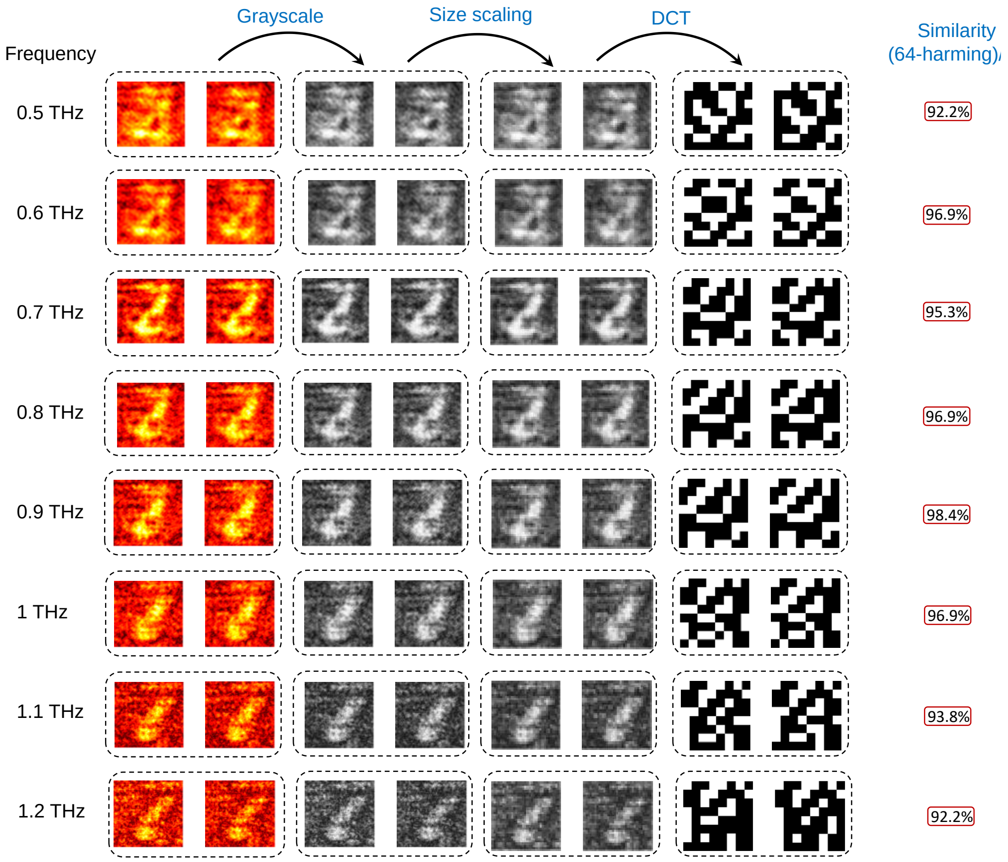

Figure S13. Experimented holograms with different frequencies on transmission and reflection space, respectively and its similarity calculation between them by pHash algorithm.

S14 Experimental system

A wave focal plane optical-pump imaging system was used to characterize the hologram imaging performance of the samples, as shown in Figure S14(a). The laser in the system is provided by a titanium sapphire regenerative amplifier manufactured by Spectra Physics, USA, with a central wavelength of 800 nm, a pulse width of 100 fs, a repetition frequency of 1 kHz, an output power of 900 mW, and a laser spot diameter of about 10 mm. This laser pulse was split into two beams and employed as the pump and probe beams to generate and detect waves. A ZnTe crystal with crystal orientation <110> was used to generate terahetz pulses through the optical rectification effect, while another ZnTe crystal with the same crystal orientation was used for detection. The CCD acquires the image information of the two polarized components, E_x and E_y, of the detected light simultaneously and matches and subtracts them for the differential detection to get final results. Here, in order to minimize the effect of noise due to laser power drift, a chopper is inserted into the pump optical path to modulate the output of wave pulses and synchronize the control with the CCD, and the wave information is extracted by subtracting two adjacent frames with and without electric field modulation. In addition, the signal-to-noise ratio (SNR) of the system can be improved by repeating the acquisition of 64 images and averaging them at each time-domain acquisition point. The time-domain signal is Fourier transformed to obtain the complex amplitude of the two-dimensional electric field at each frequency. Holograms with circular polarization (σ+/-) are obtained by synthesizing two mutually perpendicular electric field components (E_x and E_y). For testing wave signal intensity, we replaced the CCD with a terahertz probe to construct the homemade optical-pump terahertz-probe spectroscopy system system[21,22] for characterizing ultrafast dynamics. A rotary table was added to detect the modulation signals of the OEM beamformer with variable steering angles. When testing the reflective signals of samples, we adjusted the angle of the detector element to prevent the probe from blocking the incident wave from the transmitter (T). The samples were placed with a 5° inclination to spatially separate the incident wave and reflected wave in the receiver (R) region, as shown in Figure S12(c).

For tunable beam steering, we measured the tunable scattering intensity of the deflected beam at various pump fluences at 0.56 THz, as shown in Figures 4d and 4e. The scattering amplitudes are firstly obtained by scanning over the 10°~60° and −10°~−60° ranges for transmitted and reflected waves, respectively, by rotary fiber-based terahertz-TDS. The incident light was deflected to 35° and −35° by the deflector for transmission and reflection waves, respectively. We then rebuilt the OPTP system, collecting the maximum scattering intensity at ±35° to measure the tunable behavior of the OEM deflector at different pump fluences. As expected, the intensity of the deflected beam decreases as the pump fluence increases. A fluence as low as 100 μJ/cm^2 is enough to switch off the deflection radiation completely. In particular, the synchronization characteristics for transmitted and reflected waves are also observed in the tuning process.

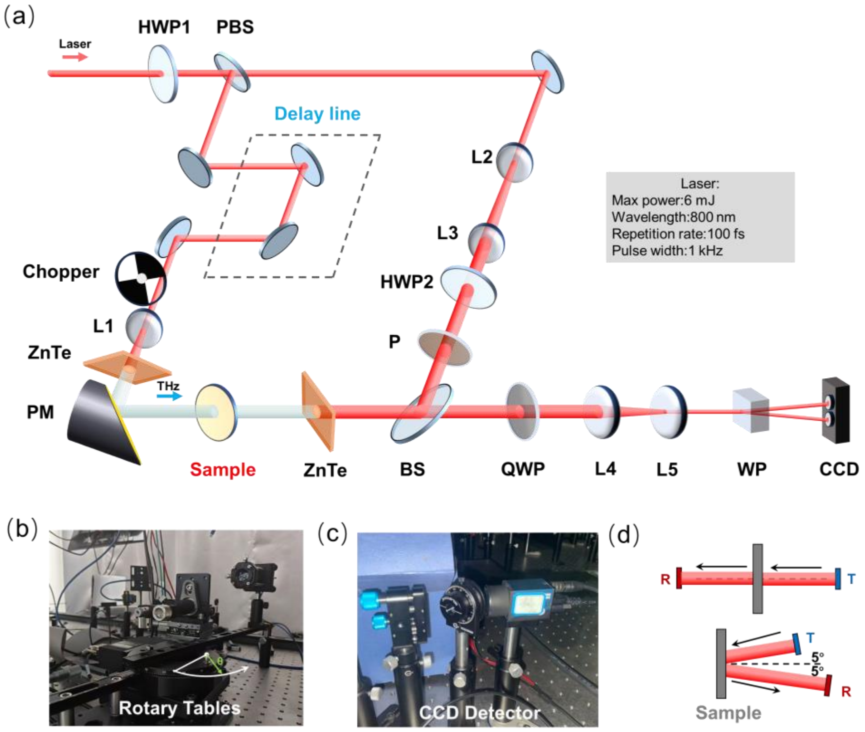

Figure S14. Laser-based wave experimental system

S15 A comparison of active EM multifunctional OEM arrays

Table S1. A comparison of active EM multifunctional OEM arrays

Ref.	Active media	Time scale[a]	Stimuli	Modulation depth	Energy need	Bandwidth, THz (relative)	Manipulation space
[9]	LC	s	Electrical	-	20 V	0.72-0.74	Reflection space
[10]	VO_2	s	Thermal/ Electrical	180° phase	20 V	0.425	Reflection space
[11]	GST	min	Thermal	-	120 mJ/cm^2	0.4-0.8 (66.7%)	Transmission space
[12]	SOS	ps	Light	85%	1.9 mJ/cm^2	0.6-1.0 (50%)	Transmission space
[13]	α-Si	ps	Light	Frequency	15 GW/cm^2	348.6±5.77 (1.6%)	Reflection space
[14]	α-Si	ps	Light	-	0.04 mJ/cm^2	0.63	Transmission space
[15]	GaN-HEMT	ns	Electrical	180° phase	10 V	0.34	Reflection space
Our work	**SOS, our work**	**ps**	**light**	**97%~83% amplitude and 360° phase**	**0.1 mJ/cm^2**	**0.51-1.21 (84.1%)**	**Full space (transmission and reflection spaces)**

S16 A comparison of frequency-scanning OEM array

Table S2. A comparison of frequency-scanning OEM array

Ref.	**Operating frequency (GHz)**	**Relative bandwidth (%)**	**Beam scanning range**	**Continuous beam scanning**	**Continuous energy control**
[16]	225-325	36.4%	14.3°	NO	NO
[17]	250-300	18.2%	12.5°	NO	YES
[18]	800-1200	22.2%	12°/23°	NO	YES
[19]	600-1800	100%	>20°	NO	YES
[20]	80-220	93.3%	25°/31.5°	NO	YES
Our work	**510-1210**	**81.4%**	**42° in four quadrants (168°)**	**YES**	**YES**

References:

[1] Costa, F., Monorchio, A., & Manara, G. (2014). An overview of equivalent circuit modeling techniques of frequency selective surfaces and OEM arrays. Appl. Comput. Electromagn. Soc. J, 29(12), 960-976.

[2] Vrejoiu, C. Electromagnetic multipoles in Cartesian coordinates. *J Phys A: Math Gen*. 35(46), 9911 (2002)

[3] Talebi, N., Guo, S., & van Aken, P. A. Theory and applications of toroidal moments in electrodynamics: their emergence, characteristics, and technological relevance. *Nanophotonics*. 7(1), 93-110 (2018)

[4] Kaelberer, T., Fedotov, V. A., Papasimakis, N., Tsai, D. P., & Zheludev, N. I. (2010). Toroidal dipolar response in a metamaterial. Science, 330(6010), 1510-1512.

[5] Shi, Z. et al. Single-layer OEM array with controllable multiwavelength functions. *Nano Lett*. 18(4), 2420-2427 (2018)

[6] Baena, J. D., Del Risco, J. P., Slobozhanyuk, A. P., Glybovski, S. B., & Belov, P. A. Self-complementary OEM arrays for linear-to-circular polarization conversion. *Phys*. *Rev*. *B*. 92(24), 245413 (2015)

[7] Song, L. Z., Zhang, T., Qin, P. Y., Du, J., & Guo, Y. J. Sub-THz Broadband Transmitting OEM arrays with Enhanced Frequency Scanning Capability. *IEEE Trans*. *Tera*. *Sci*. *Tech*. (2023)

[8] Luo, W., Sun, S., Xu, H. X., He, Q., & Zhou, L. Transmissive ultrathin Pancharatnam-Berry OEM arrays with nearly 100% efficiency. *Phys*. *Rev*. *Appl*. 7(4), 044033 (2017)

[9] Li, W., Chen, B., Hu, X., Guo, H., Wang, S., Wu, J., ... & Wu, P. (2023). Modulo-addition operation enables THz programmable OEM array for high-resolution two-dimensional beam steering. Science Advances, 9(42), eadi7565.

[10] Chen, B., Wang, X., Li, W., Li, C., Wang, Z., Guo, H., ... & Wu, P. (2022). Electrically addressable integrated intelligent THz OEM array. Science Advances, 8(41), eadd1296.

[11] Zhang, S., Chen, X., Liu, K., Li, H., Xu, Y., Jiang, X., ... & Tian, Z. (2022). Nonvolatile reconfigurable THz wave modulator. PhotoniX, 3(1), 7.

[12] Cong, L., Srivastava, Y. K., Zhang, H., Zhang, X., Han, J., & Singh, R. (2018). All-optical active THz OEM arrays for ultrafast polarization switching and dynamic beam splitting. Light: Science & Applications, 7(1), 28.

[13] Guo, X., Ding, Y., Duan, Y., & Ni, X. (2019). Nonreciprocal OEM array with space-time phase modulation. Light: Science & Applications, 8(1), 123.

[14] Zhou, H., Zhang, S., Wang, S., Yao, Y., Cai, Q., Lin, J., ... & Zhou, L. (2023). Optically controlled dielectric OEM arrays for dynamic dual-mode modulation on THz waves. Advanced Photonics, 5(2), 026005-026005.

[15] Lan, F., Wang, L., Zeng, H., Liang, S., Song, T., Liu, W., ... & Mittleman, D. M. (2023). Real-time programmable OEM array for THz multifunctional wavefront engineering. Light: Science & Applications, 12(1), 191.

[16] Yi, H., Qu, S. W., Ng, K. B., Chan, C. H., & Bai, X. (2015). 3-D printed millimeter-wave and THz lenses with fixed and frequency scanned beam. IEEE Transactions on Antennas and Propagation, 64(2), 442-449.

[17] Zheng, S., Li, C., Wu, S., Li, H., Yang, G., & Fang, G. (2021). Terahertz transmissive OEM array for realizing beam steering by frequency scanning. Journal of Lightwave Technology, 39(17), 5502-5507.

[18] Liu, S., Noor, A., Du, L. L., Zhang, L., Xu, Q., Luan, K., ... & Cui, T. J. (2016). Anomalous refraction

and nondiffractive Bessel-beam generation of THz waves through transmission-type coding OEM arrays. ACS photonics, 3(10), 1968-1977.

[19] Grady, N. K., Heyes, J. E., Chowdhury, D. R., Zeng, Y., Reiten, M. T., Azad, A. K., ... & Chen, H. T. (2013). Terahertz metamaterials for linear polarization conversion and anomalous refraction. Science, 340(6138), 1304-1307.

[20] Song, L. Z., Zhang, T., Qin, P. Y., Du, J., & Guo, Y. J. (2023). Sub-THz Broadband Transmitting OEM arrays with Enhanced Frequency Scanning Capability. IEEE Transactions on Terahertz Science and Technology.